# Self-Organized Large-Scale Integration of Mesoscale-Ordered Heterojunctions for Process-Intensified Photovoltaics

Siddharth Thakur,[1] Saptak Rarotra,[1] Mitradip Bhattacharjee,[2] Shirsendu Mitra,[1] Gayatri Natu,[2,*]
Tapas Kumar Mandal,[1,2] Ashok Kumar Dasmahapatra,[1,2,†] and Dipankar Bandyopadhyay[1,2,‡]

[1]*Department of Chemical Engineering, Indian Institute of Technology Guwahati, Assam 781039, India*
[2]*Centre for Nanotechnology, Indian Institute of Technology Guwahati, Assam 781039, India*

Self-organization of large-area nanoscale patterns employing a single-step inexpensive process can be crucial in the fabrication of low-cost but high-performance devices. In the present study, we employ the spin dewetting of a conductive polymer to fabricate an array of micro-to-nanoscale ordered-heterojunctions (OHJ) to demonstrate the improvements in the key performance indicators of organic photovoltaic (OPV) devices in ambient conditions. For this purpose, the surface of a hole-collector polymer film [e.g., (poly-(2,3-dihydrothieno-1, 4-dioxin):poly-(styrene sulfonate) (PEDOT:PSS)], coated on a transparent conducting substrate, is decorated with physicochemical patterns of a self-assembled monolayer. Afterward, the electron donor polymer [e.g., poly (3-hexylthiophene-2,5-diyl) (P3HT)] is spin-dewetted into a large collection of digitized micro- and nanodroplets. A theoretical analysis of the governing equations with appropriate boundary conditions uncovers that the imbalance of centripetal, capillary, and van der Waals forces plays a major role in deciding the droplet spacing of the spin-dewetted morphologies. Further, simulations are performed to understand the effect of size and periodicity of the donor droplets inside the device architecture, which could lead to an enhanced current flow when compared with a planar heterojunction (PHJ) device composed of thin films. Subsequently, a detailed experimental analysis is performed to uncover the role of spin speed and the initial loading of the electron donor polymer into the solvent during spin casting on the size, periodicity, and density of the electron donor droplets on the hole-collector surface. Capping the optimally discretized P3HT droplet arrays with the electron-acceptor layer [e.g., ([6,6]-phenyl-$C_{61}$ butyric acid methyl ester (PCBM)] led to the formation of a highly corrugated donor-acceptor interface suitable for higher photon absorption, facile exciton generation, and improved exciton separation. The self-organized-large-scale-integration (SOLSI) of the spin-dewetted droplets at the charge-carrier donor-acceptor interface of the OPV-OHJ assemblage enables the enhancement by approximately 40% as compared to similar OPV-PHJ configurations. The enhanced photoconversion efficiency takes place via optimal separation of photon absorption and carrier collection pathways. The study uncovers the importance of developing high-density and large-area nanopatterns employing spin dewetting to develop process-intensified OPV-OHJ cells with improved performance at a lower fabrication cost.

## I. INTRODUCTION

In recent times, the expansive optical, electronic, or mechanical properties of the dense and discrete nanostructures of diverse materials emerging from the quantum realm have been staging a paradigm shift in the performance of a variety of cutting-edge applications, which include portable memory devices, photovoltaic cells, photocatalysts, lab-on-a-chip instruments, point-of-care-testing devices, and fuel cells [1–6]. For example,

the discretization of a single unit of traditional thin-film solar cells into an array of miniaturized cells can harvest solar energy more efficiently owing to the availability of a higher surface-to-volume ratio for the superior photon absorption, electron-hole pair dissociation, and charge transport [7,8]. The merit of this proposition arises from the experimental evidence obtained for the energy harvesters with micro- or nanoscale foot-print areas, which have routinely shown improved efficiency when compared with their macroscopic counterparts. Large-scale fabrication of such mesoscale units can be one of the alternative pathways to develop the next-generation high-performance solar cell technologies [8–10]. However, one of the major limiting factors in the feasibility of such

*gayatri.natu@iitg.ac.in
†akdm@iitg.ac.in
‡dipban@iitg.ac.in

attempts is the cost associated with the existing fabrication techniques [11]. Certainly, the inventions associated with the development of simpler and economic methodologies for the large-scale fabrication of digitized micro- or nanoscale solar cells may be one significant step toward process-intensified solar-energy harvesting.

In this direction, single step, fast, simple, and inexpensive soft-lithography techniques have shown enormous potential in the past few decades [12–14]. For example, the self-organized dewetting of thin films has been employed to disintegrate thin films into the large-area digitized micro- or nanopatterns [15,16]. While a super-thin film (e.g., less than 20 nm) resting on a homogeneous surface spinodally dewets to form holes on the film with the magnification of atmospheric perturbations due to the van der Waals forces, the dewetting of the thicker films due to heterogeneous nucleation sets in through the hole-formation near the physical, or chemical defects present on a substrate [15–29]. In both mechanisms, the holes grow to form threadlike interconnected tessellations, which later undergo Rayleigh-Plateau instability to form randomly placed droplets on the substrate. The size, periodicity, and order of the dewetted patterns have been efficiently tuned when guided by physical or chemical patterns decorated on the substrates [30–38]. A number of recent studies have shown that apart from these conventional routes, the spin-dewetting of a macroscopic droplet can be another simple but inexpensive avenue to develop large-area digitized micro- and nanoscale patterns [39–41]. In the present study, we show that the self-organized spin-dewetting of conducting polymers (CPs) can indeed lead to an array of process-intensified micro- or nanoscale solar cells with improved performance.

The spin-dewetting phenomenon is found to happen conditionally during the spin coating of a thin film on a substrate. Typically, at the lower spin speed during the casting, the centripetal force together with the stabilizing capillary force help in spreading a droplet on a solvophilic flat surface to form a uniform film [42]. However, when the spin casting is performed on a solvophobic or a patterned surface with periodic topographic or chemical patterns, formation of the discrete miniaturized droplets is observed at relatively higher spin speeds [39–41]. The spin-dewetted discrete droplets originate from the combined influence of the solvophobicity, wettability gradients on the underlying

substrate, centripetal force, van der Waals interactions, and the destabilizing component of the capillary force [39–41]. In the present study, macroscopic CP droplets are spin-dewetted on the chemically patterned surfaces to develop self-organized-large-scale-integration (SOLSI) of micro- or nanoscale organic photodetectors and solar energy harvesters having improved efficiency.

Figure 1 schematically shows some of the common assemblage of solar cells, namely the planar (PHJ), bulk (BHJ), and ordered (OHJ) heterojunctions. It is now well established that the performance of a solar cell primarily depends on the efficiencies of light absorption, electron-hole pair (exciton) generation and separation, carrier diffusion and charge transport, and charge collection [43,44]. Previous studies indicate that while the PHJ configurations are very often limited by inefficient exciton separation and diffusion near the heterojunction, the random networks in BHJ can produce dead ends and isolated domains to trap charge carriers and prevent them from being extracted efficiently [45]. Interestingly, the OHJ configuration allows the structuring of one of the active components into vertically aligned structures with the size and periodicity of the order of the exciton-diffusion length, which leads to an orthogonality in the light-absorption and exciton-diffusion steps of the photovoltaic process [44,46]. In such a scenario, the photons are absorbed along the periodic patterns decorated on the donor layer, generating a high number of excitons before optimally diffusing across the patterned heterojunctions of optimal width to the acceptor layer.

In the present study, we employ spin dewetting to develop an array of micro- or nanoscale OHJ configuration targeting an improved efficiency as compared to a PHJ configuration. For this purpose, we have deliberately chosen the organic photovoltaic (OPV) devices owing to their facile assemblage, mechanical flexibility, fast energy payback time, and low cost [47–49]. The SOLSI of digitized OPV-OHJ devices developed with the spin-dewetted methodology is expected to provide higher efficiency, stability, and performance suitable for the development of diverse portable technologies such as flexible electronics, organic displays, and sensors. In order to fabricate the OPV-OHJ, initially, a glass-ITO (Indium-Tin Oxide) electrode is coated with a transparent hole-collector CP before a physicochemical pattern of the self-assembled



| | |
|---|---|
| Anode (PEDOT:PSS at ITO) | Electron acceptor (PCBM) |
| Electron donor (P3HT) | Cathode (Al) |

**(a) PHJ**

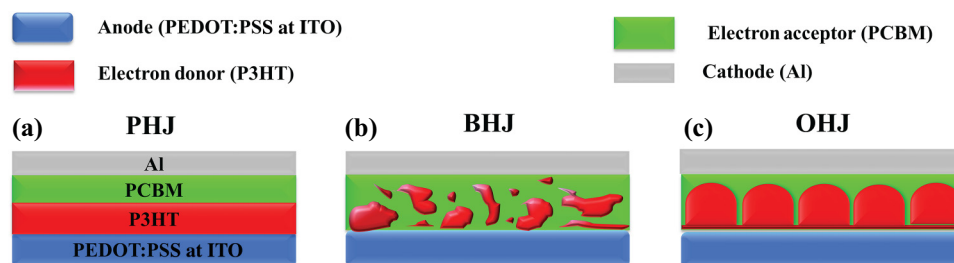| Al |
| PCBM |
| P3HT |
| PEDOT:PSS at ITO |

**(b) BHJ**

**(c) OHJ**

FIG. 1. Schematic diagram of polymeric solar cell heterojunctions. Image (a) shows the bilayer PHJ, image (b) shows a BHJ, and image (c) shows an OHJ [43].

monolayer (SAM) is decorated on the same. Thereafter, the donor CP is spin-dewetted on the patterned surface before coating the acceptor and the electrodes on the digitized donor droplets. The combination of a strong centripetal force during spin casting of the donor CP solution followed by evaporation of the solvent could create miniaturized ordered droplets with micro- or nanoscale size, periodicity, and spacing on the physicochemically heterogeneous hole-collector surface. The study uncovers the importance of developing high-density and large-area nanopatterns employing a self-organization method for improving the performance of the solar cells at a lower cost for fabrication.

The underlying physics associated with the spin-dewetting to obtain the large-area discrete patterns is also uncovered with the help of a linear stability analysis of the governing equations with the appropriate boundary conditions. The results obtained from the theoretical model suggest that the imbalance of centripetal, capillary, and van der Waals forces play a crucial role in the spacing of the spin-dewetted droplets on the hydrophilic and hydrophobic zones of the substrate. A comparison between the experimental and theoretical droplet spacing shows that, while the balance of the capillary forces decides the droplet spacing on the hydrophilic patches, the combined influence of capillary and van der Waals forces regulate the droplet spacing on the hydrophobic zones. Further, a series of computational simulations is performed to unveil the effects of device geometry and droplet arrangements on the overall current-voltage (*I-V*) characteristics of the PHJ and OHJ systems. The simulations demonstrate the advantages of the discretized geometry of the active layer over its planer arrangement.

The basic objective of constructing an OHJ-based photovoltaic device is to utilize the highly advantageous characteristics of a nano- to microscale-patterned donor CP phase. These structures possess desirable qualities such as efficient separation of electron-hole pair near the donor-acceptor junction that takes place due to the controlled size and position of poly-3hexylthiophene-2,5-diyl (P3HT) droplet phases such that they are within the exciton diffusion length of an interface, the generated charge carriers have uninterrupted pathways to their respective electrodes thereby insuring quick exit of the formed charges while avoiding dead-ends, it becomes possible to align the donor and acceptor CP phases in these kinds of architectures such that their electron and hole mobilities are enhanced, and these kind of architectures are easier to model and analyze for better understanding [43,50,51].

Importantly, the experimental results obtained from the SOLSI of the spin-dewetted discrete solar-energy harvesters are then compared and contrasted with the conventional thin-film-based polymer devices for a couple of applications such as for photodetection and solar cells. Consequently, the formed OHJ do indeed increase the shunt resistance, i.e., improve the short-circuit current, besides increasing the driving force for charge separation, i.e., improve the open-circuit voltage. The corresponding results obtained highlight the importance of the proposed way of fabrication of the active-layer morphology, which can be further utilized in solar cells for a better performance. It may be noted that, in this study, in order to show a proof-of-concept of the phenomenon discussed, the solar energy harvesters are fabricated in air rather than in a glovebox with an inert atmosphere. Further, the use of spin dewetting for the fabrication of the OPV-OHJ is found to be much simpler and more economical than the previously employed costly and complex fabrication techniques [48,52,53]. The results reported can be of significance in the development of the next-generation high-performance solar-energy harvesters at an optimal cost employing SOLSI.

## II. EXPERIMENTAL SECTION

### A. Materials

Conducting polymers PEDOT:PSS [poly-(2,3-dihydrothieno-1, 4-dioxin):poly-(styrene sulfonate)] (1.3 wt % in water), regioregular P3HT [poly (3-hexylthiophene-2,5-diyl)] (avg. Mw 15 000–45 000 gm/mol, RR > 95%) and PCBM ([6,6]-phenyl-$C_{61}$ butyric acid methyl ester) (Mw 910.88 gm/mol) are purchased from Sigma-Aldrich. The Indium Tin Oxide (ITO)-coated glasses are purchased from Global Nanotech (15 ohm/sq, >85% transmittance, $75 \times 25 \times 1.1$ mm$^3$). The quartz glass slides are purchased from Perkin-Elmer, and Cu Transmission Electron Microscopy (TEM) grids (300 mesh, 83-m pitch) are purchased from Sigma-Aldrich. The solvents and other chemicals such as chloroform, octadecyl-trichloro-silane (OTS), toluene, and dichloromethane (DCM) are procured from Merck, India. The Analytical Reagent (AR)-grade chemicals are directly used for experiments without any further purification.

### B. Characterization

Imaging ellipsometer (EP3, Nanofilm, Accurion Scientific Instruments Pvt. Ltd) is employed to measure the film thicknesses. The surface morphologies are characterized by the field emission scanning electron microscope (FESEM, Jeol India Pvt. Ltd), atomic force microscopy (AFM, Bruker, Innova series), and optical microscope (Leica, DM 2500 upright microscope). Raman spectroscopy characterization is performed by Laser micro-Raman system (Horiba Jobin Vyon, LabRam HR) with a 532-nm laser. One hundred mg aluminum of 99.997% purity is thermally evaporated onto the substrates. Keithley 2400 Source meter in connection with TS2 software is used for potentio-amperometry (*I-V*) and chronoamperometry (*I-t*) characterizations. An Oriel 200 W Xe lamp

source with an Air Mass (AM) 1.5 G filter is used for solar cell characterization, calibrated to 1 sun with a standard silicon photovoltaic cell. A 2-mW green laser excitation (532 nm) is used for photodetector characterization.

### C. Methods

Figures 2(a)–2(h) show the steps employed to assemble a SOLSI of OPV-OJH employing spin dewetting. In the beginning, the ITO substrates are cut into pieces of dimensions $1.5 \times 1.5$ cm$^2$ and are then etched to create active regions of desired dimensions. They are then cleaned according to a standard protocol as mentioned in the Sec. SI of the Electronic Supporting Information (ESI) [54]. The ITO substrates are then spin coated with a 1.3% (wt./vol) aqueous solution of PEDOT:PSS filtered through a 0.2-$\mu$m poly-vinylidene difluoride (PVDF) membrane at 2000 revolutions per minute (rpm) for 30 s. The coated substrates are heated at $140 \,^{\circ}$C for 15 min to evaporate the excess water, leading to thin-film formation of PEDOT:PSS as shown in Figs. 2(a) and 2(b). The typical thickness of the PEDOT:PSS is found to be around $120 \pm 15$ nm. Following this, PEDOT:PSS-coated ITO substrates are submerged in 10 mM (0.4 wt %) OTS in toluene solution for 7 min to form an OTS-SAM on the PEDOT:PSS surface, as shown in Fig. 2(c).

The sample is then thoroughly washed with toluene and dried employing the N$_2$ gas. After that, a 300-mesh TEM grid is placed on the OTS-SAM surface and covered with a quartz glass slide before exposing the TEM-grid-masked OTS-SAM surface to the UV-Ozone (UV-O) exposure for 30 min, as shown in Fig. 2(d) [48,55]. Due to UV-O exposure, the OTS-SAM layer is chemically converted at the uncovered patterns of the TEM grid, which was cleaned later with toluene before drying the sample with

N$_2$ gas. It may be noted here that there is a probability that the OTS-SAM layer will also dissolve with this toluene wash, which is minimized by minimizing the washing time. Consequently, the PEDOT:PSS surface is covered with physicochemically heterogeneous patterns in which the areas not exposed to UV-O had patches of solvophobic OTS-SAM while those exposed to UV-O had patches of solvophilic PEDOT:PSS, as shown in Fig. 2(e).

Following this, a P3HT in chloroform solution is spin casted on the physicochemically patterned PEDOT:PSS/OTS-SAM surface, as shown in Fig. 2(f). For studying the spin-dewetting behavior of P3HT, its concentration is varied from 0.5 to 3 mg/ml and the spin speed is varied from 1000 to 5000 rpm while the spinning duration is kept constant at 30 s. Finally, for solar-energy harvesters, a concentration of 5 mg/ml with a spin speed of 5000 rpm is used. The samples are then vacuum dried for 1 h to remove excess solvent. The spin casting of the P3HT solution on the patterned PEDOT:PSS/OTS-SAM surface led to the formation of spin-dewetted patterns owing to the presence of the lateral wettability gradient. A large collection of the P3HT droplets on the PEDOT:PSS/OTS-SAM patterned surface led to the formation of a collection of micro- or nanobatteries, which are then immediately capped off with electron-acceptor PCBM solution in dichloromethane (5 mg/ml) through spin casting at 2500 rpm for 25 s, as shown in Fig. 2(g). The excess solvent is again evaporated through rigorous vacuum drying. A 100-nm layer of Al is thermally evaporated onto the PCBM layer as the counter electrode. Figure 2(h) shows the measurement set up where the device is exposed to simulated sunlight of intensity 100 mW/cm$^2$ (Oriel 200 W –Xe lamp light source fitted with AM 1.5 G filter, intensity calibrated against a standard calibration Si solar cell), and the *I-V* characterization is done via the source meter.
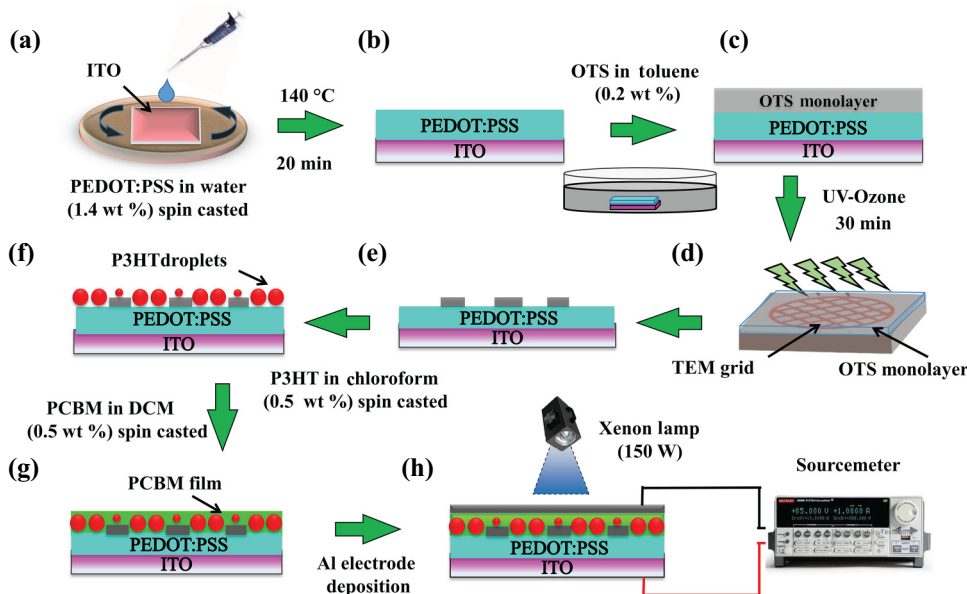


FIG. 2. Schematic diagram showing the steps to fabricate spin-dewetted conducting polymer energy-harvesting droplets on an ITO substrate. (a) spin coating of PEDOT:PSS on an ITO substrate, (b) film of PEDOT:PSS on ITO, upon heating, (c) deposition of thin OTS layer, (d) UV-O treatment of the OTS-coated surface after placing a TEM grid, (e) patterned OTS layer on the PEDOT:PSS-ITO substrate, (f) spin casting of the P3HT layer, (g) ordered spin casting of PCBM via gap filling, (h) schematic of spin-dewetted micro- nanoenergy harvester.

All the spin-coating steps are performed in a typical laboratory fume hood, with average ambient relative humidity of approximately 60%. The coated layers are dried on a hotplate with a constant flow of $N_2$ gas over the substrates. In order to find out the change in current detection capabilities of the PHJ and OHJ, we perform a visible-light detection experiment. The heterojunction devices are kept under a negative bias of 3 V and illuminated with a 2-mW laser source for a defined period of time up to 100 s. The laser illumination is "chopped" at a frequency of 0.1 Hz, i.e., the devices are illuminated for five seconds and kept in the dark for the next five seconds successively. The timestamps are collected during the potentio-amperometric scans, enabling simultaneous chronoamperometry.

## III. PROBLEM FORMULATION

### A. Linear stability analysis

In this section, a theoretical model is discussed to explain the underlying physics associated with the SOLSI through spin dewetting. Images (a)–(c) in Fig. 3 schematically describe the steps of the spin-coating process, (i) dispensing of the droplet on the substrate, (ii) rotation of the droplet, and (iii) transition of a droplet to a film, respectively. It is important to note here that modelling of the entire spin-dewetting process is cumbersome. Importantly, the experiments suggest that the droplet undergoes a large mass loss at the initial stages of rotation owing to the strong centripetal force exerted on the droplet after its placement on the spin coater, as schematically shown in images (a) and (b). However, following this incident, a film of thickness $h_i$ is formed, which is taken as the initial thickness in this theoretical model of the spin-dewetting process. We assume that this initial film thickness is a log function of
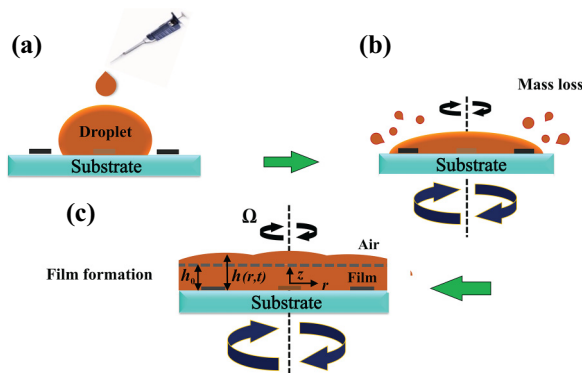


FIG. 3. Images (a)–(c) schematically describe the steps of the spin-coating process. Image (a) shows the dispensing of the droplet on the substrate, image (b) shows the rotation of the droplet, and image (c) shows the transition of a droplet to a film. The reference frame and the variables mentioned on image (c) are employed in the problem formulation. For example, a film of variable (average) film thickness, $h(r,t)$ [$h_0(t)$], is obtained when the droplet is spin cast at a spin speed of $\Omega$ on the substrate.

the spin speed, $h_i(r,t) = A + B \log \Omega$, based on the experimental observations not shown here. After the initial mass loss, the remaining liquid on the substrate of the spin coater is converted into a film, as shown in image (c), before the film spin dewets into the droplets on the substrate.

In order to develop the theoretical model of such a system, an axisymmetric cylindrical coordinate system with radial, $r$, and axial, $z$, directions is considered, as shown in the Fig. 3(c). In the formulation, a variable in bold describes a vector while a bold-variable with double over bar represents a tensor. The components of a vector are represented within a curly bracket after the bold variable. An over-dot on the variable represents a partial time derivative whereas a variable after a comma as a subscript denotes a derivative. The symbols $\bar{\bar{\mathbf{T}}}$, $\mathbf{u}\{v_r, v_\theta, v_z\}$, $\mu$, $\rho$, $\gamma$, $\Omega$, $A_e$, $p_0$, and $P(= p - \pi)$ denote the stress tensor, velocity vector, viscosity, density, surface tension, angular velocity, effective Hamaker constant, external pressure, and the excess pressure due to the intermolecular force, respectively. Material derivative and gradient operator are represented by the symbols $D$ and $\nabla$, respectively, while $\nabla_s$ represents the surface gradient operator, $\boldsymbol{I}$ represents the identity tensor, and $t$ represents time.

We assume the working fluid of approximately 0.1–0.4% (w/v) solution of P3HT in chloroform to be incompressible and Newtonian following the constitutive relation, $\bar{\bar{\mathbf{T}}} = \mu(\nabla \mathbf{u} + \nabla \mathbf{u}^T)$. The equations of motion, $\rho D\mathbf{u}/Dt = -\nabla P + \nabla \cdot \bar{\bar{\mathbf{T}}}$, along with the continuity equation, $\nabla \cdot \mathbf{u} = 0$, can describe the motion of a droplet or a film rotating under a centripetal force on the spin-coater unit, as shown in the Fig. 3(c). No slip and impermeable ($\mathbf{u} = 0$) boundary conditions are enforced at the liquid-solid interface on the substrate while the tangential ($\mathbf{n} \cdot \bar{\bar{\mathbf{T}}}_a \cdot \boldsymbol{\tau} - \mathbf{n} \cdot \bar{\bar{\mathbf{T}}} \cdot \boldsymbol{\tau} = 0$) and normal ($\mathbf{n} \cdot (-p_0\boldsymbol{I} + \bar{\bar{\mathbf{T}}}_a) \cdot \mathbf{n} - \mathbf{n} \cdot (-p\boldsymbol{I} + \bar{\bar{\mathbf{T}}}) \cdot \mathbf{n} = \gamma\kappa$) stress balances are enforced as the boundary conditions at the free liquid-air surface. Here, $\mathbf{n}\left[(-h_{,r}, 1)/\sqrt{1 + h_{,r}^2}\right]$ and $\tau\left[(1, h_{,r})/\sqrt{1 + h_{,r}^2}\right]$ represent the unit outward normal and tangent vectors at the free surface while the curvature of the deforming free surface is $\kappa = \nabla_s \cdot \mathbf{n}$. In this formulation, the notation, $h(r,t)$, denotes the film thickness and the notation, $h_0(t)$, signifies the mean film thickness while the film is under rotation. The kinematic condition at the interface is expressed as $\dot{h} + \mathbf{u} \cdot \nabla_s h = v_z$.

The governing equations and boundary conditions are then simplified under the lubrication approximation. Thus, the momentum equations reduce to the forms, $P_{,r} - \rho \Omega^2 r = \mu v_{r,zz}$ and $P_{,z} = 0$, in the $r$ and $z$ directions, respectively, while the continuity equation remains as $v_r/r + v_{r,r} + v_{z,z} = 0$. The reduced forms of tangential and normal stress balances are $v_{r,z} = 0$ and $P - p_0 - A_e/6\pi h^3 + \gamma h_{,rr} - \gamma/h = 0$. The long-wave equations of motion, continuity equation, and boundary conditions

provide analytical solutions for $v_r$ and $v_z$, which are then replaced in the kinematic equation to obtain the evolution equation for the free surface as

$$\dot{h} - \{[rh^3(P_{,r} - \rho\,\Omega^2 r)]_{,r}\}/3\mu r = 0. \qquad (1)$$

Equation (1) is then linearized using normal linear modes, $h(r,t) = h_0(t) + \tilde{h}(r)e^{\omega t + ikr}$ and $P = \bar{P} + \tilde{P}(r)e^{\omega t + ikr}$. Here, the symbols $\omega$ and $k$ represent the growth coefficient and wavenumber of perturbation and the over-tilde symbols are the perturbed variables. The base-state terms of this equation provide the relationship between the mean film thickness and the centripetal force as $\dot{h}_0 + 2\rho h_0^3 \Omega^2/3\mu = 0$, which has an analytical solution, $h_0 = \sqrt{1/[(4\rho\,\Omega^2/3\mu)t + 1/h_i^2]}$. The equation is solved under the initial condition $h_0 = h_i$ at $t = 0$. The analytical expression for the base-state thickness shows that the variation of the unperturbed film thickness before spin dewetting is a function of the time of rotation, spin speed, and initial film thickness as $h_0 = f(\Omega, t, h_i)$, which is often observed in the experiments. The expression $h_i(r,t) = A + B\log\Omega$ and a spin time of 30 s are employed with the variation in $\Omega$ to obtain the results associated with the initial film thicknesses shown here. Further, this variable base-state thickness with the spin speed has been employed to obtain the time and length scales of the spin-dewetted morphologies from the following dispersion relation, which is obtained from the perturbed-state expression of the Eq. (1) as

$$\omega = h_0^3[(A_e/2\pi h_0^4)k^2 + (\gamma/h_0^2)k^2 - \gamma k^4]/3\mu. \qquad (2)$$

The equation suggests that after thinning, the film broke down into miniaturized droplet patterns under the combined influence of the van der Waals force [first term in Eq. (2)] and capillary forces [second and third terms in Eq. (2)]. The theoretical spacing ($\lambda_m$) between the spin-dewetted droplets is obtained by evaluating $\omega_m$, the dominant growth coefficient, by setting the condition, $\partial\omega/\partial k = 0$, and then determining $\lambda_m = 2\sqrt{2}\pi/\sqrt{(A_e/2\pi h_0^4 + \gamma/h_0^2)/\gamma}$, for the dominant wavelength.

## B. Computational simulations

In order to comprehend the experimental variations in the current-voltage (*I-V*) characteristics with the change in the film or droplet arrangements at the active layer, a series of simulations are performed. In particular, we simulate a part of the proposed OPV-OHJ device structure to understand and optimize the effects of the active layer geometry on the generated electric current (*I*). The *I-V* characteristics are computationally obtained by solving the continuity equation $\nabla \cdot \mathbf{J} = 0$, the stationary form of Ohm's law, $\mathbf{J} = \sigma\mathbf{E} + \mathbf{J_e}$, and the equation for the irrotational electric field, $\mathbf{E} = -\nabla V$, where $\mathbf{J}$ is the current density, $\mathbf{J_e}$ is the externally generated current density, $\sigma$ is the electrical conductivity, $\mathbf{E}$ is the electric field, and $V$ denotes the electric-field potential. In the computations, the top and bottom boundaries of the geometry are considered as terminal and ground, respectively. Left and right boundaries are assumed to be electrically insulated. The commercially available COMSOL Multiphysics software is employed to solve the aforementioned set of governing equations and boundary conditions. The typical physical properties employed for the CP layers and SAM are tabulated in Table SI [56–62], Sec. SIII of the ESI [54]. The optimal size and spacing obtained from the simulations are employed for the applications discussed later.

## IV. RESULTS AND DISCUSSION

### A. Morphological analysis

In order to develop an array of the self-organized solar energy harvesters with the help of spin dewetting, we employ the typical electrode configuration needed for CP-based OPV devices, as shown in Fig. 2. For this purpose, the ITO-coated glass substrates are first coated with the hole collector PEDOT:PSS. Following this, a physicochemical pattern of the OTS-SAM is deposited on the PEDOT:PSS layer before a large collection of discrete micro- or nanodroplets of the donor P3HT is spin-dewetted. Figures 4(a1)–4(a4) and 4(b1)–4(b4) in rows (I) and (II) show the optical microscopic and FESEM images, respectively, of the spin-dewetted P3HT droplets on the patterned PEDOT:PSS/OTS-SAM substrate. In these images, the P3HT loading in chloroform ($C_{P3HT}$) is varied from 1 to 2.5 mg/ml while keeping the spin speed ($\Omega$) fixed at 2000 rpm. The optical micrographs, FESEM images, and the AFM images in Figs. 4(IIIa) and 4(IIIb) together corroborate a morphological transition from macro- to micro- to nanoscopic droplets with the help of spin dewetting when $C_{P3HT}$ is reduced.

Importantly, the OTS-SAM deposition on the PEDOT:PSS substrate can create three distinct zones of wettability, namely, the hydrophilic, hydrophobic, and boundary zones, as depicted in the FESEM images Figs. 4(IVa) and 4(IVb). The "box" patterns at the center have the UV-O expose the PEDOT:PSS substrate, which ensures the formation of a hydrophilic patch with larger wettability. In comparison, the peripheral area enclosing the box is hydrophobic owing to the presence of the OTS-SAM patches. A boundary zone with a gradient surface is also created in the portions where hydrophilic and hydrophobic zones merge. Spin dewetting of P3HT on the aforementioned patterned PEDOT:PSS surface leads to the formation of droplets of different sizes and spacing in the hydrophilic, hydrophobic, and boundary domains. The FESEM images in Fig. 4(IVa) show different wettability
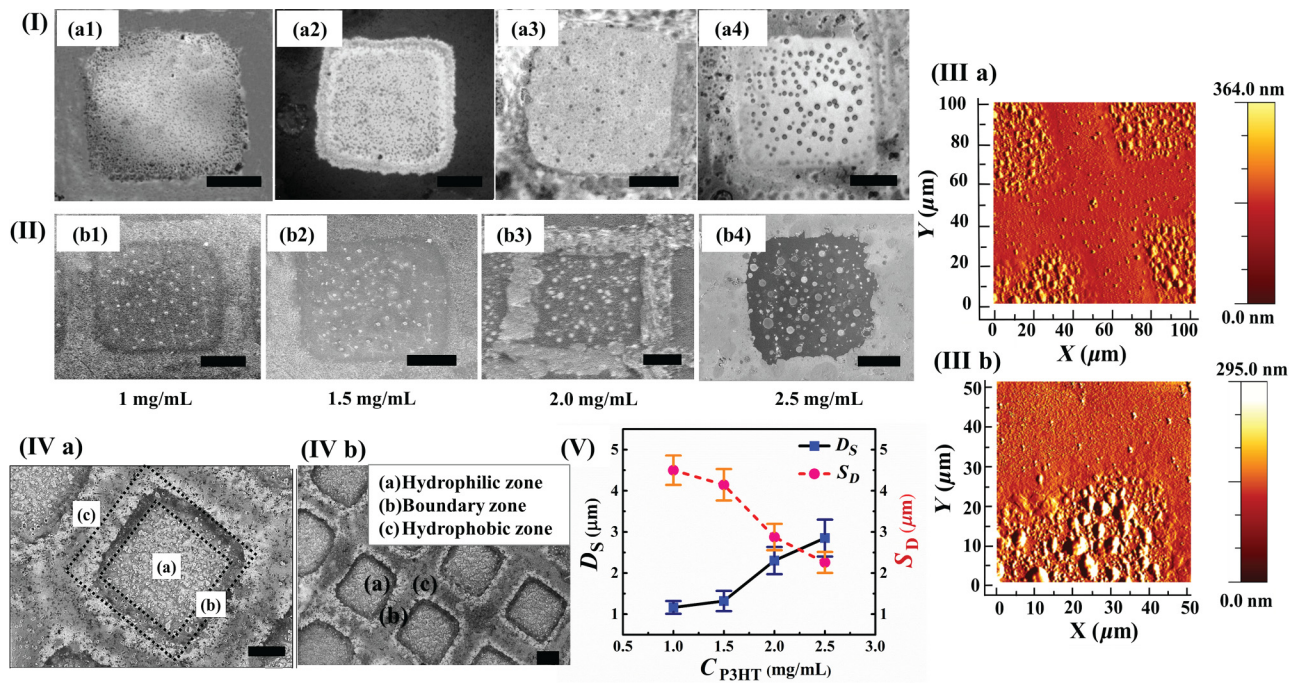
FIG. 4. Optical micrographs (I) (a1–a4) and FESEM images (II) (b1–b4) of spin-dewetted P3HT droplets at a fixed spin rate of 2000 rpm and at varying concentrations from 1 to 2.5 mg/ml. AFM images (III a) and (III b) show the topography profile of a particular case wherein P3HT concentration is fixed at 2 mg/ml and spin rate is 2000 rpm. Optical micrographs (IV a) and (IV b) shows the different zones (hydrophilic, boundary, and hydrophobic) present on the spin-dewetted P3HT patterned substrate. Plot (V) showing the variation of the average droplet diameter ($D_S$) and average droplet spacing ($S_D$) with increasing P3HT concentration. Scale bar for all the images is 20 $\mu$m.

zones at the substrate where 2 mg/ml P3HT is spin dewetted at 2000 rpm on the PEDOT:PSS/OTS-SAM substrate. Figure 4(IVb) shows the symmetric arrangements of wettability zones, namely, the hydrophilic, hydrophobic, and boundary zones, respectively, confirming SOLSI of micro- or nanodroplets increasing the overall fill factor of the same sample. Plot (V) shows the variations in the average diameter ($D_S$, $y$ axis on the left-hand side) and spacing ($S_D$, $y$ axis on the right-hand side) of the spin-dewetted P3HT droplets on the hydrophilic boxes with the change in the $C_{P3HT}$. The plot suggests a reduction in size and increase in density of the spin-dewetted droplets with the reduction in $C_{P3HT}$.

In order to uncover the particulars of the nanostructures formed during the spin dewetting of P3HT, we perform a detailed analysis based on optical microscopy and FESEM. The optical micrographs in Figs. 5(a1)–5(a5) of row (I) and the FESEM images in Figs. 5(b1)–5(b5) of row (II) show that with the increase in $\Omega$, $D_S$, and $S_D$ are both reduced on the hydrophilic and hydrophobic patches. Figures 5(IVa) and 5(IVb) show the variations in the average diameter ($D_{IA}$, $D_{OA}$) of the spin-dewetted P3HT drops in the inner and outer areas of the hydrophilic patch with $\Omega$, obtained from the FESEM images. The selection of the inner and the outer areas are depicted in Fig. 5(III). The plots suggest that, at higher spin speeds, $D_{IA}$ can be reduced to 1 from

3 $\mu$m on the hydrophilic patches, whereas $D_{OA}$ reduces from 150 to 100 nm on the hydrophobic ones. In a way, a higher spin speed helps in achieving smaller droplets with increased densities. While the miniaturization is at the microscale on the hydrophilic patches, the same is at the nanoscale on the hydrophobic ones. In fact, at higher $\Omega$, the droplets on the images are almost invisible through optical microscopy, which indicates the formation of the nanostructures.

In order to verify the presence of the material P3HT in these micro- nanodroplets decorated on the patterned PEDOT:PSS/OTS-SAM substrate, we perform Raman spectroscopy of the samples shown in Fig. 5. Figure S1 in Sec. SII of the ESI [54] confirms that the micro- nanodroplets on the patterned PEDOT:PSS/OTS-SAM substrate are indeed composed of P3HT [47,63,64]. The details of the materials' characterization have been presented with Fig. S1. The other details of the Raman spectroscopy of the different layers of organic solar cells (OSC) [65] have also been performed and the characterization results have been discussed in Sec. SII of the ESI [54].

Concisely, Figs. 4 and 5 together suggest a simple but effective way to develop an ordered array of micro- or nanoscale conducting polymer droplets on a physicochemically patterned surface, which we call SOLSI. In SOLSI, the droplet size and periodicity can be tuned
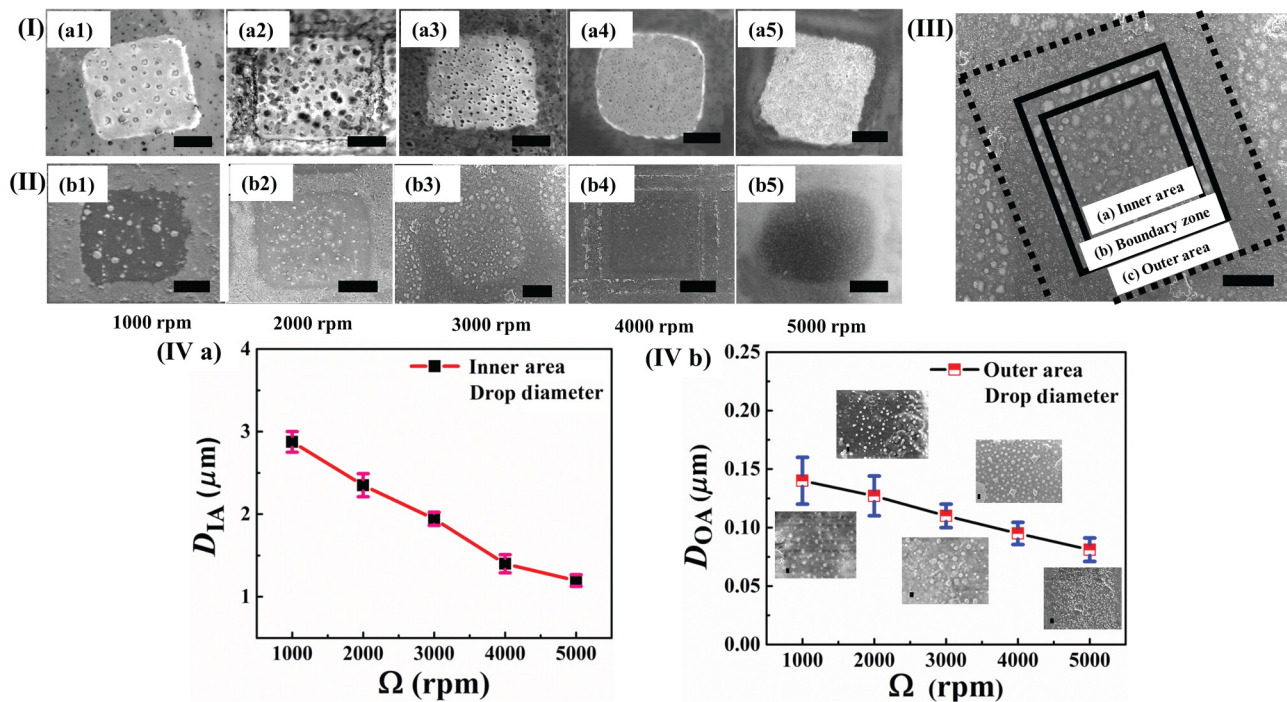
FIG. 5. Optical micrographs (I) (a1–a5) and FESEM images (II) (b1–b5) show the spin-dewetted P3HT droplets on the chemically patterned PEDOT:PSS/OTS-SAM substrate when P3HT loading in chloroform ($C_{P3HT}$) is fixed at 2 mg/ml and the spin speeds ($\Omega$) are 1000, 2000, 3000, 4000, and 5000 rpm, respectively. FESEM image (III) shows the different zones for which droplet parametric variation has been studied. Plots (IV a) and (IV b) show the variations in the avgerage droplet diameter ($D_{IA}$, $D_{OA}$) of spin-dewetted P3HT drops, in the inner areas and outer areas, with $\Omega$, respectively, obtained from the FESEM images. Scale bar for all the inner area plot images is 20 $\mu$m. Scale bar for the outer area plot images is 100 nm.

efficiently by modulating the initial-donor CP loading and the strength of the applied centripetal force. It may be noted here that eventually, the droplets generated through SOLSI are employed as a part of the active layers of OSC devices, which is discussed in the application section of this manuscript.

## B. Theoretical outlook of spin-dewetting

In the experiments, we always dispense a 100-$\mu$L droplet on the substrate before spinning the same at different speeds for 30 s to obtain the spin-dewetted morphologies. The experiments show that the droplets initially undergo a mass loss due to the centripetal force before converting into a film. As stated earlier in the theoretical section, a film of thickness $h_i$ is assumed to form after an initial mass loss, which follows a log relation with spin speed $h_i(r,t) = A + B \log \Omega$, based on the experimental observations. In the results discussed here, the constants $A$ and $B$ have two different set of values for thin films on the hydrophobic surfaces ($A = 61.22$ nm and $B = -6.5$ nm s) and thick films on the hydrophilic surfaces ($A = 1.869$ $\mu$m and $B = -0.207$ $\mu$m s). The film thus formed spreads on the substrate with the rotation of the spin coater before the same is spin dewetted under the influence of capillary and van der Waals forces. The experiments suggest that

the films become thinner with the increase in the spin speed of the coating unit before getting spin dewetted. This observation can be theoretically explained by the base-state-governing equation of the average film thickness $h_0 = f(\Omega, t, h_i) = \sqrt{1/[(4\rho \, \Omega^2/3\mu)t + 1/h_i^2]}$, where $h_i(r,t) = A + B \log \Omega$, $t = 30$ s, and $\Omega$ varies with the change in the rotational speed of the spin coater. The plots (a) and (b) in Fig. 6 show that the base-state film thickness reduces monotonically with the increase in $\Omega$, as observed in the experiments. The plots also suggest that while the average film thickness is about a few microns thick on the hydrophilic zones, the same shifts toward the nanoscopic regime on the hydrophobic zones.

As stated earlier, we employ different initial thicknesses in the dispersion relation to obtain the $\lambda_m$ vs $\Omega$ shown in plots (c) and (d) of Fig. 6. The plots suggest that the thicker films on the hydrophilic surface undergo capillary instability during the thinning process to form spin-dewetted droplets having an average periodicity ranging from 1 to 5 $\mu$m. In this situation, normalization of the dominant wavelength, $\lambda_m/h_0$, shows a constant value, 8.85, with the variation in $\Omega$, a typical signature of Plateau-Rayleigh instability, as shown in plot (c). Note that in the microdomain, the van der Waals force becomes insignificant and hence we get a Plateau-Rayleigh dominant length
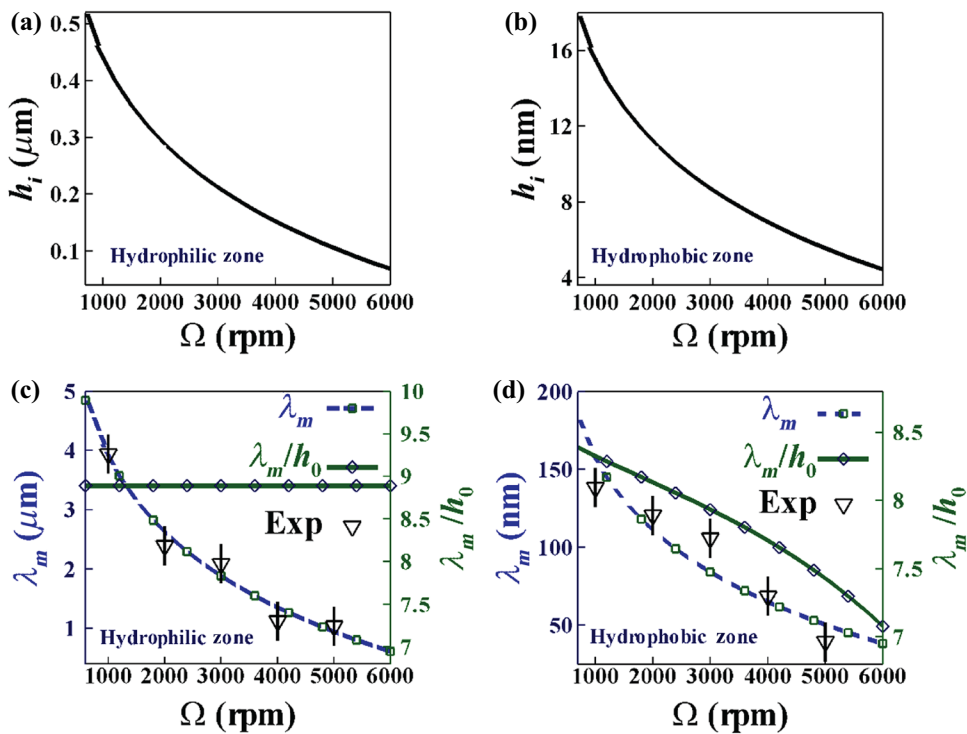
FIG. 6. The solid lines in plots (a) and (b) show the variations of the initial film thickness ($h_i$) with $\Omega$. The plots (c) and (d) show a comparison between the experimentally obtained average droplet spacing in the hydrophilic and hydrophobic zones (triangular symbols) with the theoretical one ($\lambda_m$, broken line with square symbols) when the spin speed ($\Omega$) has been varied. The plots also show the variation of parameter $\lambda_m/h_0$ (solid line with square symbols) with $\Omega$ in the two different zones. The typical parameters employed to calculate the theoretical values in the plots are $\mu = 0.038$ Pa s, $\rho = 1490$ kg/m$^3$, $\gamma = 26.1$ mN/m, $A_e = 1.7 \times 10^{-20}$ J.

scale. In comparison, the hydrophobic zones allow a thinner precursor film to form before the spin dewetting takes place. In a way, the combined influence of the van der Waals interaction and capillary forces act together to develop droplets of periodicity ranging from 40 to 150 nm, as shown in plot (d). The plot also shows that, in this case, the parameter $\lambda_m/h_0$ varies from 8.85 to 7.3 with the increase in $\Omega$, signifying the increasing influence of van der Waals interaction with the thinning for the film, as is evident in plot (d). The experimental results superimposed as triangular symbols on the theoretical predictions in plots (c) and (d) show a good agreement on the spacing of the spin-dewetted droplets. The results shown in the Fig. 6 suggest that the theoretical model is capable of predicting some of the underlying physics associated with the film formation during the spin casting of CPs and then predicting the spacing between the droplets formed after the film spin dewets following two different mechanisms on the hydrophobic and hydrophilic zones.

### C. Computational outlook on OPV

Figure 7(a) shows the geometry with the typical dimensions of the simulated device, which is very similar to the proposed experimental OPV-OHJ configuration. The *I-V* characteristics are computationally obtained by solving the equations, which is discussed in the problem formulation section above. In particular, the effects of device geometry and droplet spacing on the hydrophilic or hydrophobic zones are understood with the help of these simulations.

Cases 1–4 shown in Fig. 7 summarize the performance of the simulated planar to discrete solar cell architectures. Figure 7(b) shows the variations in the electric current for cases 1–4. For example, case 1 corresponds to a typical OPV with a thin-film configuration, while case 2 corresponds to a thin-film OPV with an OTS-SAM on the PEDOT:PSS layer. Cases 3 and 4 correspond to the different combinations of the P3HT droplets placed on the PEDOT:PSS hydrophilic patch and OTS-SAM hydrophobic patch. The number of droplets on the hydrophobic ($\alpha$ sites) and hydrophilic ($\beta$ sites) patches, respectively, are varied to study the effect of droplet position. It may be noted here that in the simulations, the discrete structures of the number of droplets on the hydrophilic and hydrophobic patches are varied after keeping the total mass of the P3HT layer the same as in the planar architecture. The simulations help in deciding the required size and spacing of the P3HT droplets for optimal *I-V* characteristics.

Since we are striving to show the advantages of the discrete active-layer geometry over the planar one, we choose the interface region between the layers to be ohmic for two reasons. First, since this is an ideal condition, the differences in the output current are only dependent on the overall interface area (interaction/exchange area) hence, the results give a clearer perspective of the better active-layer geometry. Second, models such as Richardson-Schottky and exponential trap distribution have been utilized to understand the charge transport properties in the active layer bulk. Therein, studies have reported that for lower voltages, the resistances between the layers are ohmic [66,67].
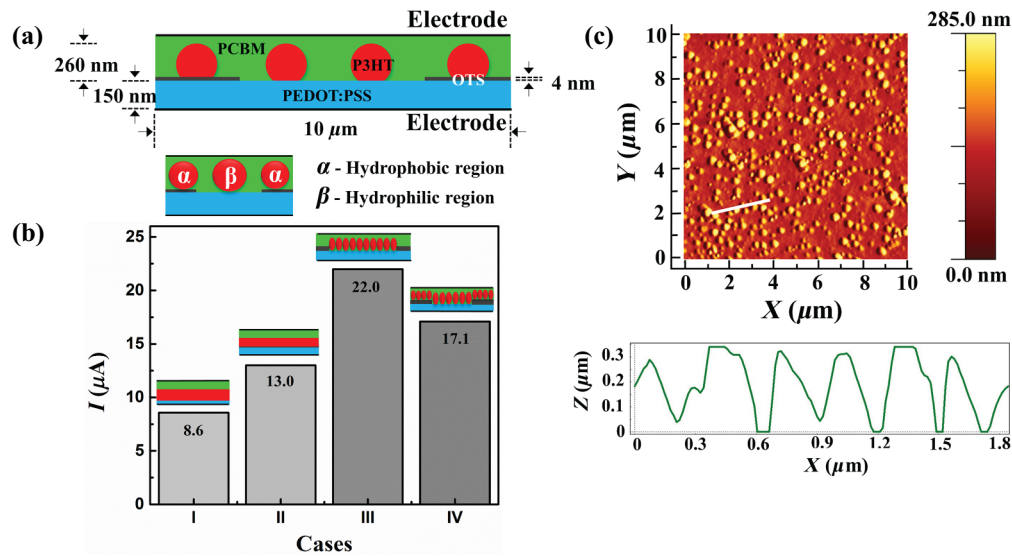
FIG. 7.    Image (a) shows the configuration of the solar cell architecture, which was analyzed with help of numerical simulations. Image (b) shows the variations in the electric current for four different cases as shown in the plot. Case 1 corresponds to a thin-film configuration, case 2 corresponds to a thin-film configuration with an OTS-SAM layer on the PEDOT:PSS surface, and cases 3–4 correspond to the different combinations of the P3HT droplets placed on the PEDOT:PSS solvophilic patch and OTS-SAM solvophobic patch. Droplets' quantities are varied on the hydrophobic ($\alpha$ sites) and hydrophilic ($\beta$ sites) patches, respectively. Case 3 incorporates a 0-10-0 configuration, which means zero P3HT droplets on the solvophobic OTS layer and 10 P3HT droplets on the solvophilic PEDOT:PSS layer and similarly for Case 4, there is a 4-6-4 configuration. Image (c) shows the AFM profile for the P3HT droplets, in the hydrophilic region, wherein the concentration is 5 mg/ml and the spin speed is 5000 rpm. Line profile displays the average droplet height across the selected white line on the AFM image.

However, for our case, we are assuming here that charges injected into the system have a negligible effect at the working voltages. The charge transport mechanism in the bulk heterojunctions of OSC is studied extensively. Studies show that major losses which contribute to the charge trapping and exciton recombination are caused due to random networks and bottlenecks present in the active layer. Hence, in order to understand the significance of an ideal system wherein charges form after separation and can directly travel to their respective electrodes, studies have modeled systems which consist of ordered columnar networks for efficient charge separation and travel. Kumar et al. have modeled a P3HT-PCBM system, wherein they have taken an ideal system comprised of networks of P3HT for hole transport and PCBM for electron transport. They have chosen this system for its simplistic nature, which inherently also suppresses the electron-hole recombination [68].

Our system configuration resembles the one mentioned above and hence validates the potential benefits of this kind of architecture. We perform a simple simulation wherein we assume the resistances between the layers and with the electrodes to be ohmic and study the significance of the change in and subsequent effect of active layer geometry on the device performance.

Hence, in order to understand the significance of the interface architecture, we perform the simulation at

a low voltage value, wherein the background charge carriers dominate the conduction compared to carriers injected by the electrodes. Although we utilize a simplified model wherein the electrical conductivity and relative permittivity of the materials determine the amount of current passing through it, our model still shows the broader picture of an active-layer interface effect on the *I-V* characteristics of the device or rather the model emphasizes the difference and significance of OHJ and PHJ.

The simulated results show that the current generated from the planar configuration in case 1 is almost 3 times less than the most efficient digitized configuration in case 3 as is evident in Fig. 7(b). This enhancement can be attributed to higher surface-to-volume-ratio of digitized P3HT droplets in case 3. For example, in case 1, the planar configuration shows a current of 8 $\mu$A, which increases to about 22.8 $\mu$A as the number of droplets are increased on the hydrophilic PEDOT:PSS patches. Previous literature suggested that the lengths for photon absorption and charge-carrier collection of the P3HT layer are approximately 300 and 10–100 nm, respectively [69]. Thus, the simulations show that the optimal height of the P3HT droplets after complete fabrication is supposed to be approximately 200–300 nm. Figure 7(c) shows the AFM image of the case of P3HT droplets with an average height of approximately 285 nm, which are obtained on the hydrophilic patch under the optimal conditions of

P3HT loading of 5 mg/ml during spin casting at 5000 rpm. The line profile provided shows the average droplet distribution with diameters having nearly equivalent values to the ones used in the simulation.

### D. Applications

In order to effectively utilize these structures for real-life applications, we employ the modified structures in active-layer regions to develop a photodetector and a solar cell. Initially, the devices are tested for their comparative efficiency in photonic detection [70]. Figure 8(a) shows the schematic set up of the device under test in the photodetector mode. As the photodetector response is measured under the third quadrant of the *I-V* curve, the device is held at a bias of -3 V. The 532-nm-laser radiation incident on the device is chopped at a frequency of 0.1 Hz for measuring the quality of the photodetection response of the device. The bar chart in Fig. 8(b)(I) indicates the average resolution of light detection from the "current ratio" [70,71], which is the measure of the difference between the current produced by the device when the laser is turned on to the situation when it is turned off. The results suggest that the discretized photodetector labeled as "OHJ" gave a better current ratio, i.e., better resolution, compared to the planar photodetector. The bar-chart in Fig. 8(b)(II) highlights the instability of the photodetectors with the variation in the starting current value in the beginning of detection until the last cycle. It is clearly seen that the OHJ configuration is able to hold the "current ratio" stable for much longer times, i.e., it is much more temporally stable than the PHJ configuration.

The considerable difference between the two can be correlated with the variation in the thin-film morphologies between the two different architectures. For OHJ, pathways for electron movement do not significantly inhibit their overall transition from the active layer to the electrodes. However, there are bottlenecks and dead-ends due to absence of any ordered structure in the PHJ, which harbors residual charges leading to unwanted charge transfer between the source and drain. Figure 8(c) indicates the decrease in the photocurrent over a period of 100 s, which confirms that the digitized photodetector has long-term stability and outperforms the planar architecture. The photocurrent seems to decrease over the given time period at a slightly faster rate. However, this can be understood by addressing the fact that all solar cell devices in this study are fabricated under ambient conditions. Under these conditions, charge-carrier extraction is not efficient due to the quick degradation of the top aluminum contact, which leads to the low fill factor (i.e., quick degradation of the photocurrent). However, as both the control (PHJ) and the OHJ devices are fabricated under identical conditions, the comparison between their overall efficiencies, short-circuit currents, and open-circuit voltages is still meaningful. The dark current profiles as shown in Fig. S2, Sec. SIV of the ESI [54] are quite different than the photocurrent profiles, and show the behavior expected from organic PV cells.

The experiments suggest that the discrete donor-acceptor junctions inhibit the decay of exciton scattering leading to a more stable photocurrent for a longer duration. The experiments shown in the Fig. 8 confirm the utility of the spin-dewetted OHJ assemblage for an efficient photodetection.

Since the new morphology of the dewetted structures presents an improved performance over its planar counterpart for light-detection phenomena, we further extend the utility of this discovery to applications in solar cells. Here, it may be pertinent to note that we perform an experiment in order to show the change in resistance across the active and nonactive regions of the device under different conditions in order to address the issue of the usage of
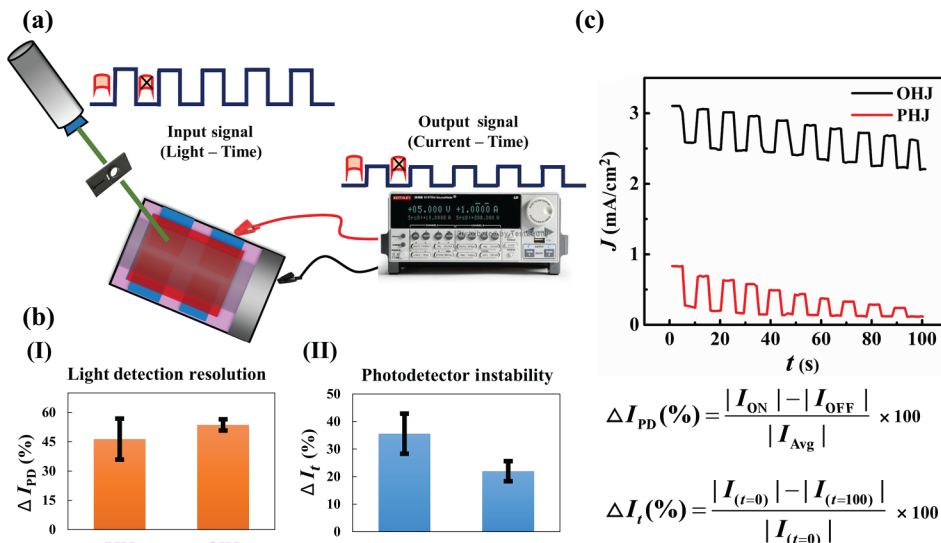


FIG. 8. Image (a) describes the schematic of the photodetector set up. Image (b) displays the chart for two parameters of photodetection phenomena: average stability of photodetector ($\Delta I_t$) and average resolution of light detection ($\Delta I_{PD}$) for two different configurations, continuous PHJ and discrete OHJ morphologies of the P3HT layer. The incident light intensity is 2 mW and the source is at a distance of 15 cm from the cell. Plot (c) shows the current-time plot obtained for the PHJ- and OHJ-based photodetectors.

$$\Delta I_{PD}(\%) = \frac{|I_{ON}| - |I_{OFF}|}{|I_{Avg}|} \times 100$$

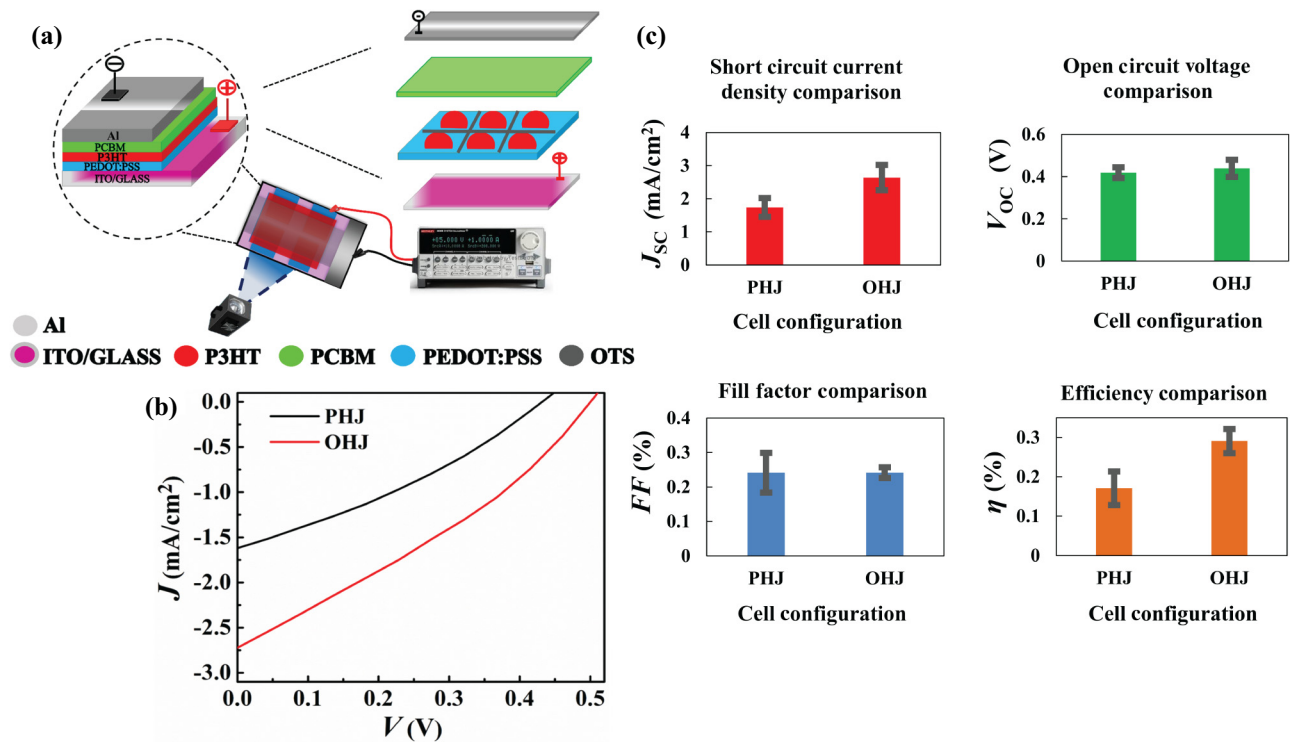$$\Delta I_t(\%) = \frac{|I_{(t=0)}| - |I_{(t=100)}|}{|I_{(t=0)}|} \times 100$$

FIG. 9.  (a) Schematic diagram of the solar cell measurement with the break-up of layers presented in the inset. The P3HT sublayer is disintegrated into a SOLSI of the micro- or nanoscale droplets. Plot (b) shows the typical *I-V* characteristics of solar cells comprising PHJ and discrete OHJ morphologies of the P3HT sublayer, obtained under simulated solar radiation of 1 sun (100 mW/cm$^2$) intensity. The fabrication and measurement of all cells are obtained outside a glovebox, under ambient conditions. Image (c) displays the average values of different characteristics of the solar cells with varying morphologies from PHJ to discrete OHJ P3HT sublayer profiles. Plots correspond to the open-circuit voltage ($V_{OC}$), short-circuit current density ($J_{SC}$), fill factor (FF), and efficiency ($\eta$), respectively. In all the cases, the initial P3HT loading before spin dewetting is 5 mg/ml and the spin speed during spin casting is 5000 rpm.

nonconducting OTS monolayers and its subsequent effect on the overall device performance. The results have been presented in Table SII, Sec. V of the ESI [54]. Herein, as can be observed from the table, the different layers give different resistances, although their values do not differ by much. However, the OTS-covered PEDOT:PSS layer presents the highest resistance value within the given system of materials. This is likely due to its nonconducting nature, although the resistance is improved to some extent after being treated by UV-O. The difference between the UV-O-treated OTS layer and the bare PEDOT:PSS-covered substrate is not much. Hence, the resistance of the nonactive regions is higher than that the active region, but the difference in values is not great.

The schematic diagram of the proposed solar cell assemblage is described in Fig. 9(a). It may again be noted here that, in order to show a proof-of-concept, the solar-energy harvesters reported here are fabricated in air rather than in a glovebox with an inert atmosphere. Therefore, the absolute values of key characteristics such as efficiency and fill factor are similar to those obtained during the early stages of development of OPV [72,73]. The variations in

*I-V* characteristics of the planar (PHJ) and discrete (OHJ) solar cells are shown in Fig. 9(b). Images (a) and (b) in Fig. S2, Sec. SIV of the ESI [54] show the typical *I-V* curves obtained for the OHJ and PHJ samples under dark conditions and also the best performing ones under the light exposure.

The *I-V* plot helps in obtaining the maximum power ($P_m = V_m J_m$), which is the limit of electrical power to be obtained from the solar cells when connected to an external load for the planar (PHJ) and discrete (OHJ) solar cells. Thereafter, the fill factor, $FF = 100[(V_m I_m)/(V_{OC} I_{SC})]$ and efficiency, $\eta = V_{OC} I_{SC} FF/P_{in}$, of the planar (PHJ) and discrete (OHJ) solar cells are calculated with the help of the above formulas wherein $P_{in}$ is the incident radiant power, as shown in Fig. 9(c). The figure suggests that the SOLSI of the OHJ morphologies of P3HT-PCBM layers exhibit a marked increase in the short-circuit photocurrent ($J_{SC}$) as compared to PHJ. This is because the patterned OPV-OHJ morphology causes an overall improvement in charge-carrier extraction as expected from the architecture. An enhancement in the open-circuit photovoltage ($V_{OC}$) of the discrete OPV-OHJ as compared to the planar OPV-OHJ

points toward a higher driving force for spatial separation of the charge carriers in the SOLSI of spin-dewetted discrete solar cells [74]. This feature might also arise from the patterning enforced on the PCBM layer during spin casting owing to the presence of an array of spin-dewetted P3HT islands. The overall lower values of the efficiencies of the devices can be attributed to the fabrication and characterization of the cells under ambient conditions. However, even under this scenario, a 40% increase in the solar cell efficiency is obtained for the OPV-OHJ configurations as compared to OPV-PHJ.

## V. CONCLUSIONS

We show here a facile and economic top-down pathway to fabricate an array of high-density spin-dewetted conducting polymer patterns suitable for photodetection and photovoltaic applications. In order to show a proof-of-concept, initially the surface of a hole-collector conducting polymer (e.g., PEDOT:PSS) is coated with the pattern of a self-assembled monolayer before spin dewetting an array of ordered micro- or nanoscale droplets of an electron-donor conducting polymer (e.g., P3HT). The configuration is chosen to develop patterned active-layer morphologies for preparing OHJ organic solar cells. Droplet size, spacing, and density are tuned by altering the initial P3HT loading during spin dewetting and the strength of the applied centripetal force. We establish a simple theoretical model for spin dewetting of the donor CP solution to determine the experimental spacing between the droplets on hydrophobic and hydrophilic surfaces. A computational study is performed to understand the significance of droplet geometry and its morphological density with respect to the active-layer morphology. The P3HT micro- or nanodroplets are then utilized for a light-detection application wherein OHJ morphologies perform comparatively better against PHJ with lower instability and matching light-detection resolution. The OHJ of P3HT layer is further applied as a part of the active layer of an OSC, which shows a superior performance when compared against the PHJ. A significant increase in the active area and much reduced effective charge-transfer pathway are attributed to this enhanced performance. The difference in the results in the plain to discrete morphologies of OSCs provides a cue on the usage of the highly dense and ordered active layers in improving the performance of the various thin-film-based photovoltaic applications.

## ACKNOWLEDGMENTS

[1] C. Tan, Z. Liu, W. Huang, and H. Zhang, Non-volatile resistive memory devices based on solution-processed ultrathin two-dimensional nanomaterials, Chem. Soc. Rev. **44,** 2615 (2015).

[2] C. Clavero, Plasmon-induced hot-electron generation at nanoparticle/metal-oxide interfaces for photovoltaic and photocatalytic devices, Nat. Photonics **8,** 95 (2014).

[3] Y. Shi, C. Hua, B. Li, X. Fang, C. Yao, Y. Zhang, Yong-Sheng Hu, Z. Wang, L. Chen, D. Zhao, and G. D. Stucky, Highly ordered mesoporous crystalline MoSe$_2$ material with efficient visible-light-driven photocatalytic activity and enhanced lithium storage performance, Adv. Funct. Mater. **23,** 1832 (2013).

[4] J. Heinemann, K. Deng, S. C. C. Shih, J. Gao, P. D. Adams, A. K. Singh, and T. R. Northen, On-chip integration of droplet microfluidics and nanostructure-initiator mass spectrometry for enzyme screening, Lab Chip **17,** 323 (2017).

[5] A. Gao, N. Lu, Y. Wang, and T. Li, Robust ultrasensitive tunneling-fet biosensor for point-of-care diagnostics, Sci. Rep. **6,** 22554 (2016).

[6] N. R. Elezovic, V. R. Radmilovic, and N. V. Krstajic, Platinum nanocatalysts on metal oxide based supports for low temperature fuel cell applications, RSC Adv. **6,** 6788 (2016).

[7] Y. Yang, K. Mielczarek, M. Aryal, A. Zakhidov, and W. Hu, Nanoimprinted polymer solar cell, ACS Nano **6,** 2877 (2012).

[8] M. Aryal, K. Trivedi, and W. Hu, Nano-confinement induced chain alignment in ordered p3ht nanostructures defined by nanoimprint lithography, ACS Nano **3,** 3085 (2009).

[9] D. Chen, W. Zhao, and T. P. Russell, P3ht nanopillars for organic photovoltaic devices nanoimprinted by aao templates, ACS Nano **6,** 1479 (2012).

[10] X. He, F. Gao, G. Tu, D. Hasko, S. Hüttner, U. Steiner, N. C. Greenham, R. H. Friend, and W. T. S. Huck, Formation of nanopatterned polymer blends in photovoltaic devices, Nano Lett. **10,** 1302 (2010).

[11] T. Ito and S. Okazaki, Pushing the limits of lithography, Nature **406,** 1027 (2000).

[12] P. Kim, K. W. Kwon, M. Cheol Park, S. Hoon Lee, S. M. Kim, and K. Yang Suh, Soft lithography for microfluidics: A review, Biochip J. **2,** 1 (2008).

[13] Y. Xia and G. M. Whitesides, Soft lithography, Annu. Rev. Mater. Sci. **28,** 153 (1998).

[14] S. H. Kang and M. D. Dickey, Patterning via self-organization and self-folding: Beyond conventional lithography, MRS Bull. **41,** 93 (2016).

[15] P. G. de Gennes, Wetting: Statics and dynamics, Rev. Mod. Phys. **57,** 827 (1985).

[16] G. Reiter, Dewetting of Thin Polymer Films, Phys. Rev. Lett. **68,** 75 (1992).

[17] M. Sferrazza, M. Heppenstall-Butler, R. Cubitt, D. Bucknall, J. Webster, and R. A. L. Jones, Interfacial Instability Driven by Dispersive Forces: The Early Stages of Spinodal Dewetting of a Thin Polymer Film on a Polymer Substrate, Phys. Rev. Lett. **81,** 5173 (1998).

[18] R. Xie, A. Karim, J. F. Douglas, C. C. Han, and R. A. Weiss, Spinodal Dewetting of Thin Polymer Films, Phys. Rev. Lett. **81,** 1251 (1998).

[19] R. V. Craster and O. K. Matar, Dynamics and stability of thin liquid films, Rev. Mod. Phys. **81,** 1131 (2009).

[20] R. Mukherjee and A. Sharma, Instability, self-organization and pattern formation in thin soft films, Soft Matter **11,** 8717 (2015).

[21] A. Sharma, Relationship of thin film stability and morphology to macroscopic parameters of wetting in the apolar and polar systems, Langmuir **9,** 861 (1993).

[22] J. Bischof, D. Scherer, S. Herminghaus, and P. Leiderer, Dewetting Modes of Thin Metallic Films: Nucleation of Holes and Spinodal Dewetting, Phys. Rev. Lett. **77,** 1536 (1996).

[23] S. H. Lee, P. J. Yoo, S. J. Kwon, and H. H. Lee, Solvent-driven dewetting and rim instability, J. Chem. Phys. **121,** 4346 (2004).

[24] J. K. Bal, T. Beuvier, A. B. Unni, E. A. Chavez Panduro, G. Vignaud, N. Delorme, M. S. Chebil, Y. Grohens, and A. Gibaud, Stability of polymer ultrathin films (<7 nm) made by a top-down approach, ACS Nano **9,** 8184 (2015).

[25] A. Beena Unni, G. Vignaud, J. K. Bal, N. Delorme, T. Beuvier, S. Thomas, Y. Grohens, and A. Gibaud, Solvent assisted rinsing: Stability/instability of ultrathin polymer residual layer, Macromolecules **49,** 1807 (2016).

[26] R. Konnur, K. Kargupta, and A. Sharma, Instability and Morphology of Thin Liquid Films on Chemically Heterogeneous Substrates, Phys. Rev. Lett. **84,** 931 (2000).

[27] A. Sehgal, D. Bandyopadhyay, K. Kargupta, A. Sharma, and A. Karim, From finite-amplitude equilibrium structures to dewetting in thin polymer films on chemically patterned substrates, Soft Matter **8,** 10394 (2012).

[28] A. Oron, S. H. Davis, and S. G. Bankoff, Long-scale evolution of thin liquid films, Rev. Mod. Phys. **69,** 931 (1997).

[29] G. Reiter, A. Sharma, A. Casoli, M.-O. David, R. Khanna, and P. Auroy, Thin film instability induced by long-range forces, Langmuir **15,** 2551 (1999).

[30] A. M. Higgins and R. A. L. Jones, Anisotropic spinodal dewetting as a route to self-assembly of patterned surfaces, Nature **404,** 476 (2000).

[31] R. Mukherjee, D. Bandyopadhyay, and A. Sharma, Control of morphology in pattern directed dewetting of thin polymer films, Soft Matter **4,** 2086 (2008).

[32] B. Yoon, H. Acharya, G. Lee, H.-C. Kim, J. Huh, and C. Park, Nanopatterning of thin polymer films by controlled dewetting on a topographic pre-pattern, Soft Matter **4,** 1467 (2008).

[33] N. Bhandaru, A. Das, and R. Mukherjee, Confinement induced ordering in dewetting of ultra-thin polymer bilayers on nanopatterned substrates, Nanoscale **8,** 1073 (2016).

[34] G. G. Baralia, C. Filiâtre, B. Nysten, and A. M. Jonas, Nanodecoding by dewetting, Adv. Mater. **19,** 4453 (2007).

[35] D. Julthongpiput, W. Zhang, J. F. Douglas, A. Karim, and M. J. Fasolka, Pattern-directed to isotropic dewetting transition in polymer films on micropatterned surfaces with differential surface energy contrast, Soft Matter **3,** 613 (2007).

[36] M. Ghezzi, S. C. Thickett, and C. Neto, Early and intermediate stages of guided dewetting in polystyrene thin films, Langmuir **28,** 10147 (2012).

[37] U. Thiele, L. Brusch, M. Bestehorn, and M. Bär, Modelling thin-film dewetting on structured substrates and templates: Bifurcation analysis and numerical simulations, Eur. Phys. J. E **11,** 255 (2003).

[38] D. Bandyopadhyay, A. Sharma, S. W. Joo, and S. Qian, Self-organized micropatterning of thin viscous bilayers under microgravity, Microgravity Sci. Technol. **22,** 273 (2010).

[39] N. Ferrell, A. Bross, and D. Hansford, Micro/nanofabrication by spin dewetting on a poly(dimethylsiloxane) mold, Mater. Res. Soc. Symp. Proc. **1002-N05-11** (2011).

[40] N. Bhandaru, A. Das, N. Salunke, and R. Mukherjee, Ordered alternating binary polymer nanodroplet array by sequential spin dewetting, Nano Lett. **14,** 7009 (2014).

[41] B. Ravi, S. Chakraborty, M. Bhattacharjee, S. Mitra, A. Ghosh, P. S. Gooh Pattader, and D. Bandyopadhyay, Pattern-directed ordering of spin-dewetted liquid crystal micro- or nanodroplets as pixelated light reflectors and locomotives, ACS Appl. Mater. Interfaces **9,** 1066 (2017).

[42] W. W. Flack, D. S. Soong, A. T. Bell, and D. W. Hess, A mathematical model for spin coating of polymer resists, J. Appl. Phys. **56,** 1199 (1984).

[43] A. C. Mayer, S. R. Scully, B. E. Hardin, M. W. Rowell, and M. D. McGehee, Polymer-based solar cells, Mater. Today **10,** 28 (2007).

[44] L. Lu, T. Zheng, Q. Wu, A. M. Schneider, D. Zhao, and L. Yu, Recent advances in bulk heterojunction polymer solar cells, Chem. Rev. **115,** 12666 (2015).

[45] N. Banerji, Pushing the knowledge of interfaces, Nat. Mater. **16,** 503 (2017).

[46] A. Polman, M. Knight, E. C. Garnett, B. Ehrler, and W. C. Sinke, Photovoltaic materials: Present efficiencies and future challenges, Science **352,** aad4424 (2016).

[47] J. Razzell-Hollis, W. C. Tsoi, and J.-S. Kim, Directly probing the molecular order of conjugated polymer in opv blends induced by different film thicknesses, substrates and additives, J. Mater. Chem. C **1,** 6235 (2013).

[48] N. Herzer, M. M. Wienk, P. Schmit, A. B. Spoelstra, C. E. Hendriks, S. D. Oosterhout, S. Hoeppener, and U. S. Schubert, Fabrication of pedot-ots-patterned ito substrates, J. Mater. Chem. **20,** 6618 (2010).

[49] D. Joshi, R. Shivanna, and K. S. Narayan, Organic photovoltaics: Key photophysical, device and design aspects, J. Mod. Opt. **61,** 1703 (2014).

[50] E. C. Garnett, M. L. Brongersma, Y. Cui, and M. D. McGehee, Nanowire solar cells, Annu. Rev. Mater. Res. **41,** 269 (2011).

[51] K. M. Coakley, Y. Liu, C. Goh, and M. D. McGehee, Ordered organic–inorganic bulk heterojunction photovoltaic cells, MRS Bull. **30,** 37 (2011).

[52] E. Menard, M. A. Meitl, Y. Sun, J.-U. Park, D. J.-L. Shir, Y.-S. Nam, S. Jeon, and J. A. Rogers, Micro- and nanopatterning techniques for organic electronic and optoelectronic systems, Chem. Rev. **107,** 1117 (2007).

[53] A. F. Lasagni, J. L. Hendricks, C. M. Shaw, D. Yuan, D. C. Martin, and S. Das, Direct laser interference patterning of poly(3,4-ethylene dioxythiophene)-poly(styrene sulfonate) (pedot-pss) thin films, Appl. Surf. Sci. **255,** 9186 (2009).

[54] See Supplemental Material at http://link.aps.org/supplemental/10.1103/PhysRevApplied.10.064012 — for more details about the ITO substrate cleaning procedure, Raman characterization of the different layers of the OSC, values of different physical properties employed in the COMSOL simulations, I-V curves obtained for the OHJ and PHJ samples under dark condition and also the ones which performed best under the light exposure and the I-V curves for the OTS/PEDOT:PSS layers.

[55] N. Herzer, R. Eckardt, S. Hoeppener, and U. S. Schubert, Sample target substrates with reduced spot size for maldi-tof mass spectrometry based on patterned self-assembled monolayers, Adv. Funct. Mater. **19,** 2777 (2009).

[56] J. Obrzut and K. A. Page, Electrical conductivity and relaxation in poly(3-hexylthiophene), Phy. Rev. B **80,** 195211 (2009).

[57] Y. Shen and M. C. Gupta, in 38th IEEE Photovoltaic Specialists Conference (2012), p. 002770.

[58] S. S. Kim, S. Bae, and W. H. Jo, Performance enhancement of planar heterojunction perovskite solar cells by n-doping of the electron transporting layer, Chem. Commun. **51,** 17413 (2015).

[59] F. Jahani, S. Torabi, R. C. Chiechi, L. J. A. Koster, and J. C. Hummelen, Fullerene derivatives with increased dielectric constants, Chem. Commun. **50,** 10645 (2014).

[60] J. Saghaei, A. Fallahzadeh, and M. H. Yousefi, Improvement of electrical conductivity of PEDOT:PSS films by 2-Methylimidazole post treatment, Org. Electron **19,** 70 (2015).

[61] P. John, I. M. Odeh, and J. Wood, The electrical conductivity of polysilane, J. Chem. Soc., Chem. Commun., 1496 (1983).

[62] F. Gala and G. Zollo, Dielectric properties of self-assembled monolayer coatings on a (111) silicon surface, J. Phys. Chem. C **119,** 7264 (2015).

[63] S. H. Chang, C. H. Chiang, F. S. Kao, C. L. Tien, and C. G. Wu, Unraveling the enhanced electrical conductivity of pedot:pss thin films for ito-free organic photovoltaics, IEEE Photon. J **6,** 1 (2014).

[64] Y.-K. Han, M.-Y. Chang, W.-Y. Huang, H.-Y. Pan, K.-S. Ho, T.-H. Hsieh, and S.-Y. Pan, Improved performance of polymer solar cells featuring one-dimensional pedot nanorods in a modified buffer layer, J. Electrochem. Soc. **158,** K88 (2011).

[65] S. Berhanu, F. Tariq, T. Jones, and D. W. McComb, Three-dimensionally interconnected organic nanocomposite thin films: Implications for donor-acceptor photovoltaic applications, J. Mater. Chem. **20,** 8005 (2010).

[66] Y. Shen, K. Li, N. Majumdar, J. C. Campbell, and M. C. Gupta, Bulk and contact resistance in P3ht:Pcbm heterojunction solar cells, Sol. Energy Mater. Sol. Cells **95,** 2314 (2011).

[67] Rashmi, K. K. Ashok, S. Annapoorni, and K. Vikram, Conduction mechanisms in poly(3-hexylthiophene) thin-film sandwiched structures, Semicond. Sci. Technol. **23,** 035008 (2008).

[68] P. Kumar, S. C. Jain, V. Kumar, S. Chand, and R. P. Tandon, A model for the j-v characteristics of P3ht:Pcbm solar cells, J. Appl. Phys. **105,** 104507 (2009).

[69] S. Moungthai, N. Mahadevapuram, P. Ruchhoeft, and G. E. Stein, Direct patterning of conductive polymer domains for photovoltaic devices, ACS Appl. Mater. Interfaces **4,** 4015 (2012).

[70] S. Li, D. Xue, W. Xu, Y. Feng, J. Wang, G. Zhang, X. Meng, C. Wang, Y. Song, and C. Shu, Improving the photo current of the [60]pcbm/p3ht photodetector device by using wavelength-matched photonic crystals, J. Mater. Chem. C **2,** 1500 (2014).

[71] Z. Jin and J. Wang, High-responsivity solution-processed organic-inorganic hybrid bilayer thin film photoconductors, J. Mater. Chem. C **1,** 7996 (2013).

[72] G. Yu, J. Gao, J. C. Hummelen, F. Wudl, and A. J. Heeger, Polymer photovoltaic cells: Enhanced efficiencies via a network of internal donor-acceptor heterojunctions, Science **270,** 1789 (1995).

[73] J. J. M. Halls, K. Pichler, R. H. Friend, S. C. Moratti, and A. B. Holmes, Exciton diffusion and dissociation in a poly(p-phenylenevinylene)/c60 heterojunction photovoltaic cell, Appl. Phys. Lett. **68,** 3120 (1996).

[74] K. Vandewal, S. Himmelberger, and A. Salleo, Structural factors that affect the performance of organic bulk heterojunction solar cells, Macromolecules **46,** 6379 (2013).